Reprinted from

Methods in Geochemistry and Geophysics, 35

THREE-DIMENSIONAL ELECTROMAGNETICS

Proceedings of the Second International Symposium

Edited by

Michael S. ZHDANOV

and

Philip E. WANNAMAKER
University of Utah
Salt Lake City
UTAH, U.S.A.

2002
ELSEVIER
Amsterdam - Boston - London - New York - Oxford - Paris
San Diego - San Francisco - Singapore - Sydney - Tokyo

Chapter 8

THREE-DIMENSIONAL MAGNETOTELLURIC MODELING AND INVERSION: APPLICATION TO SUB-SALT IMAGING

Gregory A. Newman [a], G. Michael Hoversten [b] and David L. Alumbaugh [c]

[a] *Sandia National Laboratories, Albuquerque, NM 87185, USA*
[b] *Lawrence Berkeley National Laboratory, Berkeley, CA 94729, USA*
[c] *University of Wisconsin-Madison, Madison, WI 53706, USA*

Abstract: Three-dimensional (3D) magnetotelluric (MT) forward and inverse solutions are reviewed and applied in a resolution study for sub-salt imaging of an important target in marine magnetotellurics for oil prospecting. In the forward problem, finite-difference methods are used to efficiently compute predicted data and cost functional gradients. A fast preconditioner is introduced at low induction numbers to reduce the time required to solve the forward problem. We demonstrate a reduction of up to two orders of magnitude in the number of Krylov sub-space iterations and an order of magnitude reduction in time needed to solve a series of test problems. For the inverse problem, we employ a nonlinear conjugate gradient solution developed on massively parallel computing platforms. Solution stabilization is achieved with Tikhonov regularization. To further improve the image resolution of sub-salt structures, we have also incorporated two additional constraints within the inversion process. The first constraint allows for the preservation of known structural boundaries within the inverted depth sections. This type of constraint is justified for the sub-salt imaging problem because the top of salt is constrained by seismic data. The other constraint employed places variable lower bounds on the electrical conductivity above and below the top of salt. Cross-sections of the inversion results over the center of the salt structures indicate that the 3D analysis provides somewhat more accurate images compared to faster 2D analysis, but is computationally much more demanding. On the flanks of the structures, however, 3D analysis is necessary as 2D inversion shows image artifacts arising from the 3D nature of the data. We conclude, however, that 3D inversion may not be cost effective for the sub-salt imaging problem. Very fine data sampling along multiple profiles employed in the 3D analysis yielded only a marginal improvement in image resolution compared to 2D analysis along carefully selected data profiles. The study also indicates that in order to provide resolution that is required to accurately define the base of the salt, additional constraints beyond that employed here, need to be incorporated into the 3D inversion process.

1. INTRODUCTION

With the advent of multiple channel 24 bit data acquisition systems, the ability to acquire large amounts of high-quality magnetotelluric (MT) data is rapidly becoming a reality. This is evidenced by our ability to acquire MT data sets in remote and harsh marine environments (cf. Constable et al., 1998; Hoversten et al., 2000). Accompanying this advance in data acquisition technology has been a significant improvement in the data processing capabilities, including the introduction of a remote reference to reduce bias associated with noise in the magnetic field measurements (Gamble et al., 1979) and robust transfer function response estimation (cf. Egbert and Booker, 1986). Because of these improvements in instrument accuracy and data processing, MT surveys are starting to be designed where data are acquired along several parallel profiles rather than just along one or two which has been traditionally the case. The use of multiple lines allows for three-dimensional (3D) geological structures to be better delineated.

Paralleling the improvement in data acquisition systems has been the increasing speed and memory capability of computers. This has allowed for the development of algorithms that more accurately take into account some of the multi-dimensionality of the MT interpretation problem. For example 2D MT inversion schemes that 10 years ago required a Cray computer for reasonable computation times (cf. DeGroot-Hedlin and Constable, 1990) can now run in a period of a few minutes to an hour or two on standard desktop workstations and PCs. In addition computationally efficient algorithms have been developed that either make subtle approximations to the 2D problem (cf. Smith and Booker, 1991; Siripunvaraporn and Egbert, 2000) or that use efficient iterative gradient algorithms (cf. Rodi and Mackie, 2001) to produce 2D images of the geological structure.

In 3D environments, 2D interpretation of the data is standard practice because of quick processing times and because of the scarcity and time consuming nature of 3D MT modeling and inversion schemes. Thus one may never fully know the advantages, if any, 3D MT inversion can offer without actually applying it to the data. Moreover in some 3D environments it is conceivable that the use of 2D interpretation schemes may result in artifacts appearing in the images that could lead to misinterpretation. Therefore there exists a need for efficient 3D forward modeling and inversion algorithms to be developed. In this paper we outline recent progress that has been made in developing one such set of algorithms (Newman and Alumbaugh, 2000), and employ them on a simulated petroleum exploration problem.

The exploration problem we have selected to demonstrate these algorithms is a resolution study for imaging the base of 3D salt structures. Such structures are encountered in petroleum exploration in the Gulf of Mexico, where seismic imaging beneath these high-velocity formations is a formidable task. The scattering of seismic energy produced by these formations limits the ability of migration methods to delineate the base of salt as well as deeper oil bearing horizons. Additional motivation for pursuing such a study is to compare the 3D results with the 2D MT work already done on the problem (cf. Hoversten et al., 1998, 2000). If 3D data analysis shows significant improvements in our ability to image sub-salt structures, it could justify the extra time and cost needed to acquire and interpret the 3D MT data sets.

Before presenting the resolution study, details on the 3D forward and inversion algorithms employed in the investigation are discussed. This is necessary in order to document the changes we made to the algorithms in the course of this study. The first change we will discuss is the development of a low-frequency preconditioner needed to greatly reduce the computation time required in the forward problem at long periods.

MT simulations at periods greater than 1000 s are used in the resolution study due to the highly conductive seawater and sea sediments, and the new preconditioner has a significant impact in reducing computational run times at the longer periods. The other changes correspond to the incorporation of additional constraints, beyond the standard Tikhonov regularization employed for constructing smooth solutions to the inverse problem. Specific constraints to be discussed include preservation of known structural boundaries, such as the top of salt, within the inverted depth sections, and incorporation of variable lower bounding constraints on the electrical conductivity above and below the top of salt. It will be shown that incorporation of these constraints into the MT inverse problem improves our ability to image the base of salt.

2. THE 3D MT FORWARD PROBLEM

2.1. Governing equations and solution

In solving the 3D MT inverse problem it is critical that the forward-modeling solution simulates the responses arising from realistic 3D geology. Parameterizations of hundreds of thousands of cells are typically required for these types of numerical simulations. Hence highly efficient solution techniques are required. Here we employ finite-difference modeling techniques for the task as outlined in Newman and Alumbaugh (2000).

Assuming a harmonic time dependence of $e^{i\omega t}$, where $i=\sqrt{-1}$ and ω is the angular frequency, the electric field, $\mathbf{E}$, satisfies the vector equation

$$\nabla \times \nabla \times \mathbf{E} + i\omega\mu_o\sigma\mathbf{E} = \mathbf{0}. \tag{8.1}$$

In this expression the electrical conductivity is denoted by σ and μ_o represents the magnetic permeability of free space. Note, the equation can be arranged such that the magnetic permeability is also variable (cf. Alumbaugh et al., 1996), but for simplicity we have assumed it to be constant. Dirichlet boundary conditions are applied to Equation (8.1), where the tangential electric-field boundary values are specified on the boundaries of a large prism that includes the investigation domain (the earth) as well as the air. These boundary values arise from a plane wave, with a given source-field polarization, propagating in layered or 2D geologic media assigned at the boundaries of the 3D problem.

When Equation (8.1) is approximated with finite differences using a Yee (1966) staggered grid and symmetrically scaled (Newman and Alumbaugh, 1995), a linear system results:

$$\mathbf{KE} = \mathbf{S}. \tag{8.2}$$

The matrix $\mathbf{K}$ is complex-symmetric and sparse with 13 non-zero entries per row and $\mathbf{S}$ is the source vector that depends on the boundary conditions and source-field polarization. This system can be efficiently solved at moderate to high induction frequencies using the quasi-minimum residual (qmr) method with Jacobi preconditioning; solution treatment at low frequencies will be given below. The qmr algorithm belongs to the class of

Krylov sub-space techniques that are highly efficient in iteratively solving sparse linear systems. The reader is referred to Newman and Alumbaugh (1995) for the details on how the solver is implemented. Once the electric fields are determined on the mesh, the magnetic fields, $\mathbf{H}$, can be determined from Faraday's law,

$$\mathbf{H} = \nabla \times \mathbf{E} / -i\omega\mu_o, \tag{8.3}$$

by numerically approximating the curl of the electric field at the nodal points. One can then interpolate either the electric or magnetic field nodal values to the detector location. At this point the magnetotelluric impedance tensor, including apparent resistivity and phase are readily computed from the electric and magnetic fields.

2.2. Preconditioning

It is well known that difficulties will be encountered when attempts are made to solve Equation (8.2) as frequencies approach the static limit (cf. Smith, 1996; Newman and Alumbaugh, 2000). In this section we will show how these difficulties can be overcome, with preconditioning. The preconditioner that we will introduce parallels the work of Druskin et al. (1999), who developed a new spectral Lanczos decomposition method (SLDM) with Krylov sub-spaces generated from the inverse of the Maxwell operator. We have successfully implemented it for reducing solution times in induction logging problems (Newman and Alumbaugh, 2002). Here we derive it for MT applications.

Following Druskin et al. (1999) we assume that the electric field can be decomposed into curl-free and divergence-free projections via the Helmholtz theorem, where

$$\mathbf{E} = \mathbf{\Psi} + \nabla\varphi \tag{8.4}$$

and

$$\nabla \cdot \mathbf{\Psi} = 0 \tag{8.5}$$

Substituting Equations (8.4) and (8.5) into Equation (8.1), and using the vector identity

$$\nabla \times \nabla \times \mathbf{\Psi} = -\nabla^2\mathbf{\Psi}, \tag{8.6}$$

along with the fact that $\nabla \cdot \mathbf{\Psi} = 0$ and $\nabla \times \nabla \times \nabla\varphi = 0$, we arrive at

$$-\nabla^2\mathbf{\Psi} + i\omega\mu_o\sigma(\mathbf{\Psi} + \nabla\varphi) = \mathbf{0}. \tag{8.7}$$

Splitting the electric field into curl-free and divergence-free projections removes the null space of the curl–curl operator in the solution process. When Krylov methods are applied directly to Equation (8.2), this null space is responsible for the poor convergence properties of the solution process as frequency approaches the static limit.

To develop an approximate finite-difference solution to Equation (8.1) at low frequencies, we first estimate the relative sizes of the curl–curl and attenuation operators in Equation (8.1) assuming a finite-difference approximation. Let Δ be the characteristic grid size employed in the finite-difference mesh, then the size of the discrete curl–curl operator is roughly, $1/\Delta^2$, whereas the size of the attenuation operator is approximated as $\omega\mu_o\sigma$. Thus as frequency falls and the grid size is reduced we observe the condition that

$$1/\Delta^2 \gg \omega\mu_o\sigma_{\max} \tag{8.8}$$

or

$$1 \gg \Delta^2 \omega \mu_o \sigma_{\max}, \tag{8.9}$$

where $\sigma_{\max}$ is the maximum conductivity in the mesh. When the finite-difference grid is non-uniform, Δ should be replaced by $\Delta_{\max}$, the maximum cell size used to approximate Equation (8.1). Assuming Equation (8.9) is satisfied, Equation (8.7) can then be decoupled such that

$$-\nabla^2 \mathbf{\Psi} = \mathbf{0}. \tag{8.10}$$

Note that the right hand side of Equation (8.9) is a dimensionless *induction number* (cf. Frischknecht, 1987), which has important implications on the validity of Equation (8.10) and thus the effectiveness of the preconditioner introduced below. More importantly, notice that Equation (8.9) also indicates the importance of the cell size employed within the mesh, in addition to the frequency and conductivity. Thus Equation (8.10) may apply even at moderate to high frequencies (up to 100s of kHz) as long as the grid size employed for the problem is sufficiently small. This property has allowed for the beneficial use of the preconditioner in solving induction logging problems (Avdeev et al., 2002), where very small cell sizes are employed to model a borehole.

The boundary conditions required to solve Equation (8.10) are a mixture of Dirichlet and Neumann types. Dirichlet conditions are applied to the tangential components of $\mathbf{\Psi}$ on the mesh boundaries ($\mathbf{\Psi}_t$ has to be specified). For the normal components, Neumann conditions are applied, where $\partial \mathbf{\Psi}_n / \partial n$ is specified with the constraint that $\nabla \cdot \mathbf{\Psi} = 0$ is discretely satisfied on the mesh boundaries and in turn within the solution domain because the divergence-free field is required to satisfy the constraint equation

$$\nabla^2 (\nabla \cdot \mathbf{\Psi}) = 0. \tag{8.11}$$

Equation (8.11) follows by applying the divergence operator to Equation (8.6). It is well known that when the scalar function, $u = \nabla \cdot \mathbf{\Psi}$, satisfies Laplace's equation, $\nabla^2 u = 0$, on some domain Ω with homogeneous boundary conditions of $u = 0$ prescribed along the boundary Γ, it is identically zero on that domain. Note when applying the Neumann boundary condition, n would specify the direction of the outward normal at the boundary. Thus Equation (8.5) is implicitly enforced with the solution of Equation (8.10).

The vector field $\mathbf{\Psi}$ is not a complete solution to Maxwell's equations since it does not satisfy the auxiliary divergence condition on the current density within the earth. To derive this condition we take the divergence of Equation (8.7) and arrive at

$$\nabla \cdot \sigma \nabla \varphi = -\nabla \cdot \sigma \mathbf{\Psi}. \tag{8.12}$$

Dirichlet boundary conditions will be applied to the discrete version of Equation (8.12), where φ has to be specified on the mesh boundaries; here we assume that $\varphi = 0$. When the air–earth interface is present, however, we employ the Neumann condition, $\partial \varphi / \partial n = 0$, where n again specifies the direction of the outward normal at that interface. This later boundary condition enforces the constraint that current cannot leak from the earth into the air at induction frequencies; frequencies typically less than 1 MHz.

An approximate solution to Equation (8.1) can be obtained at very small induction numbers by first solving Equation (8.10) followed by Equation (8.12) using a staggered finite-difference grid along with conjugate gradient methods. However the real benefit of using this approximation is as a preconditioner for Equation (8.2) in order to obtain a faster solution. This preconditioning involves solving the modified problem

$$\mathbf{M}^{-1}\mathbf{K}\mathbf{E} = \mathbf{M}^{-1}\mathbf{S}, \tag{8.13}$$

where $\mathbf{M}$ is chosen such that $\mathbf{M}^{-1}\mathbf{K}$ approximates the identity matrix (Greenbaum, 1997). This condition will be implicitly satisfied at low induction numbers with the solutions of Equations (8.10) and (8.12). It is important to note that the preconditioning matrix, $\mathbf{M}$, is never actually computed during the preconditioning step, only its effect upon a vector (a matrix–vector multiplication) is needed. We now describe how this is done.

During each iteration of the preconditioned qmr algorithm we substitute the residual, defined by $\mathbf{r} = \mathbf{K}\mathbf{E} - \mathbf{S}$ into the right hand side of the discrete version of Equation (8.10), where $\boldsymbol{\Psi}_{\mathrm{t}}$ and $\partial\boldsymbol{\Psi}_{\mathrm{n}}/\partial n$ are set to zero on the mesh boundary. Equations (8.10) and (8.12) are then progressively solved using conjugate gradient techniques along with an incomplete Cholesky factorization. Furthermore, the solutions to Equations (8.10) and (8.12) need not be precise, as test examples have indicated that a crude solution to these equations will still provide a significant impact on reducing the time required for solving Equation (8.2). In Appendix A, we re-derive this low induction number (LIN) preconditioner using a Neumann series expansion. From this series, we are able to provide a rigorous bound on its effectiveness as well as develop higher-order versions.

2.3. Forward model example

To demonstrate the accuracy of the solution, and show the benefits of the preconditioner, we have employed a 0.1 S/m block within a 0.01 S/m half-space. The block's dimensions are 200 m on a side and its depth of burial is 100 m below the surface on which the fields are to be measured. The size of the grid employed in this simulation was 28 cells in x and y by 36 cells in z. The minimum cell size at the center of the grid was 25 m by 25 m by 6.25 m, while at the edges of the grid the largest cell employed was 200 m by 200 m by 200 m. In Figure 1 the apparent resistivities (ρ_{xy}) at 4 Hz and 400 Hz are presented both for the finite-difference solution as well as the integral equation solution of Xiong (1992). In both cases the responses are determined at 25 m increments on the surface over the block, with agreement to within one percent.

In Figure 2, we demonstrate the effectiveness of the preconditioner at 4 Hz. A speed up approaching a factor of 7 is demonstrated compared to a solution employing simple Jacobi scaling for preconditioning; the machine employed in these comparisons is an IBM RS 590 workstation. When the LIN preconditioner is compared with the static-divergence correction procedure of Smith (1996), it is still a factor of 3 faster. At a frequency of 400 Hz, the preconditioner is still effective, but its benefits are not as great, now the speed up is only a factor of 2.

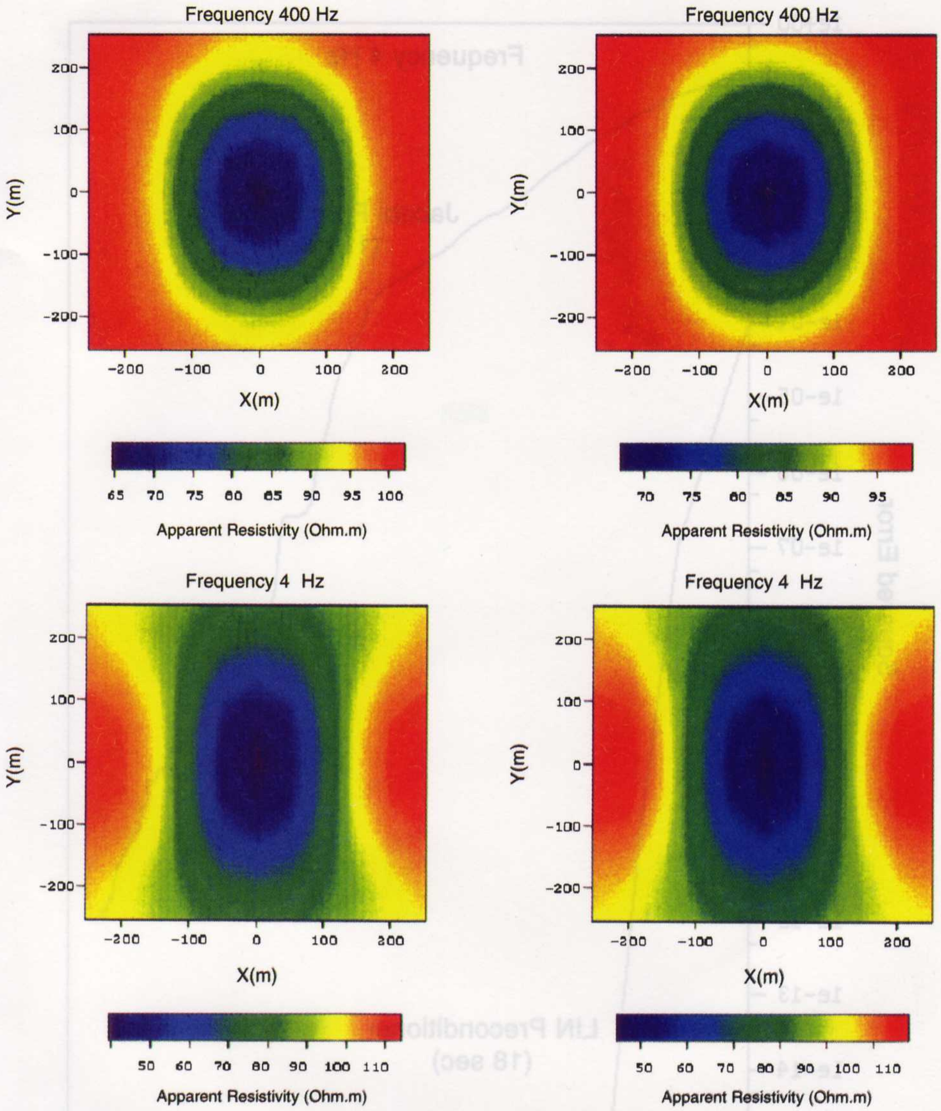

Figure 1. Comparison of finite-difference solution (apparent resistivities at 400 and 4 Hz) with the integral equation solution of Xiong (1992). The finite-difference solution is shown to the right and the integral equation solution to the left.

3. THE 3D MT INVERSE PROBLEM

3.1. Regularized least squares

Following Newman and Alumbaugh (2000), we divide the 3D earth into M cells and assign to each cell an unknown conductivity value. Let $\mathbf{m}$ be a vector of length M that

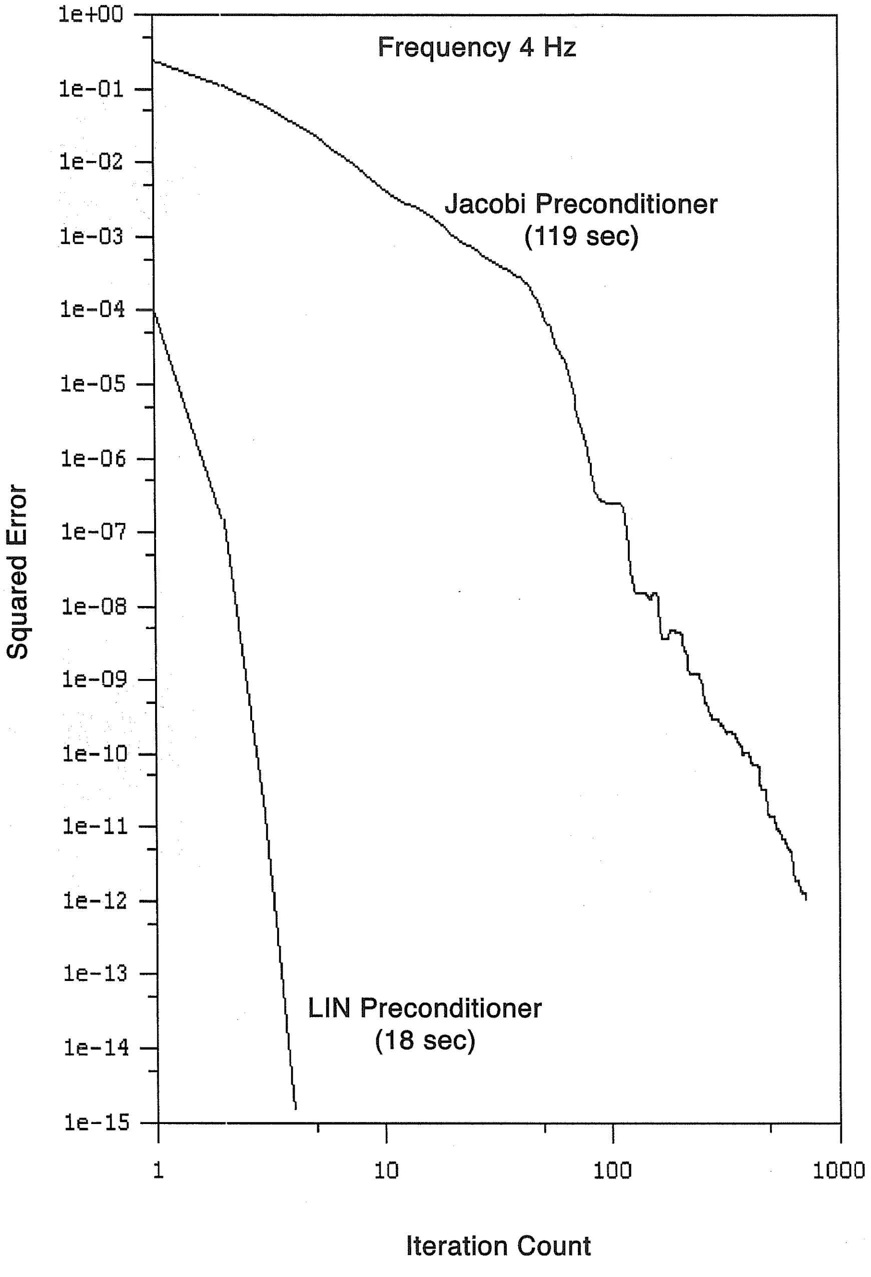

Figure 2. Convergence rates for different preconditioners, where the squared error is defined as $||KE - S||^2/||S||^2$.

describes these values. The cost functional to be minimized in the inversion process, which combines the data error and model smoothness constraint, will be given by

$$\varphi = \{\boldsymbol{\varepsilon}^{-1}(\mathbf{Z}^{\mathrm{obs}} - \mathbf{Z}^{\mathrm{pre}})\}^{\mathsf{H}}\{\boldsymbol{\varepsilon}^{-1}(\mathbf{Z}^{\mathrm{obs}} - \mathbf{Z}^{\mathrm{pre}})\} + \lambda \mathbf{m}^{\mathrm{T}}\mathbf{W}^{\mathrm{T}}\mathbf{W}\mathbf{m}, \tag{8.14}$$

where H denotes the Hermitian operator. In Equation (8.14), $\mathbf{Z}^{\mathrm{obs}}$ and $\mathbf{Z}^{\mathrm{pre}}$ are data vectors that represent the predicted and observed magnetotelluric impedances at different frequencies and locations. These are complex values, and a given entry in the data vector can represent any component of the impedance tensor,

$$\mathbf{Z} = \begin{pmatrix} Z_{xx} & Z_{xy} \\ Z_{yx} & Z_{yy} \end{pmatrix}. \tag{8.15}$$

For a description of the tensor properties as well as how they are derived, see Vozoff (1991). Finally $\boldsymbol{\varepsilon}^{-1}$ in Equation (8.14) is a diagonal matrix that contains the inverse of the data error estimates. Thus noisier data are given smaller weight, or less importance, when forming φ, than good quality data.

The regularization parameters that stabilize the inverse problem (Tikhonov and Arsenin, 1977) enforce a model smoothness constraint. Other constraints are available, some of which will be discussed below, but we employ this particular constraint here because it produces properties in the solution that we desire. In Equation (8.14) the regularization parameters are given by the matrix $\mathbf{W}$, which consists of a finite-difference approximation to the Laplacian (∇^2) operator, and the tradeoff parameter λ. This later parameter is used to control the amount of smoothness to be incorporated into the model. In its selection, we note that a large parameter will produce a highly smooth model, but this model will show poor dependence on the data. A small parameter, on the other hand, will give a superior data fit, but the resulting model may be too rough and non-physical. Following Newman and Alumbaugh (2000), Equation (8.14) is minimized multiple times with different tradeoff parameters that are fixed, and the smoothest model that provides an acceptable match to the data within observational errors is selected as the optimal result.

3.2. Nonlinear conjugate gradients

Because of the size of the inverse problem, gradient methods are the only practical means of solution. The method of steepest descent is the easiest and simplest to implement of the gradient methods. Unfortunately it usually converges very slowly in practice. A better approach is the method of nonlinear conjugate gradients, first proposed by Fletcher and Reeves (1964) for nonlinear optimization, and later improved by Polyak and Ribière (1969) and recently implemented in 2D and 3D MT inversion algorithms (cf. Newman and Alumbaugh, 2000; Rodi and Mackie, 2001). The method is closely related to the linear CG method of Hestenes and Stiefel (1952) and is in fact identical if the objective functional is quadratic. Listed below is a flowchart of the Polyak and Ribière algorithm, that will be used in the analysis to estimate the conductivity model, $\mathbf{m}^*$, which will minimize Equation (8.14).

NLCG Algorithm

```
(1)    set $i = 1$, choose initial model $\mathbf{m}_{(i)}$ and compute $\mathbf{r}_{(i)} = -\nabla\varphi(\mathbf{m}_{(i)})$
(2)    set $\mathbf{u}_{(i)} = \mathbf{M}_{(i)}^{-1}\mathbf{r}_{(i)}$
(3)    find $\alpha(i)$ that minimizes $\varphi(\mathbf{m}_{(i)} + \alpha_{(i)}\mathbf{u}_{(i)})$
(4)    set $\mathbf{m}_{(i+1)} = \mathbf{m}_{(i)} + \alpha_{(i)}\mathbf{u}_{(i)}$ and $\mathbf{r}_{(i+1)} = -\nabla\varphi(m_{(i+1)})$
(5)    Stop when $|\mathbf{r}_{(i+1)}|$ is sufficiently small, otherwise go to step (6)
(6)    set $\beta_{(i+1)} = (\mathbf{r}_{(i+1)}^{\mathrm{T}}\mathbf{M}_{(i+1)}^{-1}\mathbf{r}_{(i+1)} - \mathbf{r}_{(i+1)}^{\mathrm{T}}\mathbf{M}_{(i)}^{-1}\mathbf{r}_{(i)})/\mathbf{r}_{(i)}^{\mathrm{T}}\mathbf{M}_{(i)}^{-1}\mathbf{r}_{(i)}$
(7)    set $\mathbf{u}_{(i+1)} = \mathbf{M}_{(i+1)}^{-1}\mathbf{r}_{(i+1)} + \beta_{(i+1)}\mathbf{u}_{(i)}$
(8)    set $i = i + 1$ and go to step (3)
```

We define $\mathbf{M}_{(i)}^{-1}$ and $\mathbf{M}_{(i+1)}^{-1}$ as preconditioning matrices for all i. To use the NLCG method requires that we carefully implement two calculations of the procedure efficiently. These are (1) calculate the gradient of the cost functional, $\nabla\varphi(\mathbf{m})$, and (2) find the value of α that minimizes the expression $\varphi(\mathbf{m} + \alpha\mathbf{u})$ for specified model parameters $\mathbf{m}$ and a given conjugate search direction $\mathbf{u}$. Such procedures along with the specification of the preconditioners can be found in Newman and Alumbaugh (2000), including a massively parallel implementation of the algorithm.

3.3. Solution stabilization via additional constraints

It is commonly known that the MT inverse problem is inherently ill posed. The instability of the problem arises because the problem is underdetermined and the data sets that are used are undersampled and noisy. While regularization discussed above can stabilize the problem by omitting solutions that are not geologically reasonable, incorporation of a priori knowledge can significantly reduce remaining non-uniqueness. In fact, the choice of the Laplacian operator to form $\mathbf{W}$ can be thought of as a form of a priori knowledge as the inversion scheme will only search for smoothly varying models as acceptable solutions. Here, we have allowed three other types of a priori information about the model to be incorporated into the inversion algorithm. As it will be demonstrated later in this paper, addition of a priori information can help improve the resolution of the MT inverse problem.

The first constraint we introduce is to invert against a reference model, $\mathbf{m}_{\mathrm{ref}}$, where we now minimize

$$\varphi = \{\boldsymbol{\varepsilon}^{-1}(\mathbf{Z}^{\mathrm{obs}} - \mathbf{Z}^{\mathrm{pre}})\}^{\mathrm{H}}\{\boldsymbol{\varepsilon}^{-1}(\mathbf{Z}^{\mathrm{obs}} - \mathbf{Z}^{\mathrm{pre}})\} + \lambda(\mathbf{m} - \mathbf{m}_{\mathrm{ref}})^{\mathrm{T}}\mathbf{W}^{\mathrm{T}}\mathbf{W}(\mathbf{m} - \mathbf{m}_{\mathrm{ref}}). \tag{8.16}$$

Justification for this type of constraint is that in many cases we have prior information on the geological units that we expect to encounter in a survey. Inverting against a reference model refines this information with the constraint that an acceptable fit to the data can be achieved. Another useful constraint is to incorporate ‘tears’ in the smoothing matrix W (cf. Hoversten et al., 1998). This constraint applies when we know the location of a boundary surface between two regions of contrasting conductivity. An example of this situation occurs in marine magnetotellurics when determining the base of sub-salt structures. Here the top of salt is known independently from seismic data and this information can be used to better restrain the base of salt that is to be estimated in the MT inversion process. A third type of a priori knowledge involves lower-bound constraints, which allow the user to designate the lowest conductivity value that the model can attain on a cell by cell basis. This constraint is actually implemented by inverting for the logarithm of the parameters and also insures that the conductivity is positive, which is a physical requirement. Following Newman and Alumbaugh (1995), let us introduce a new parameter n_k that is related to the kth model parameter, m_k using a natural logarithm transformation as follows:

$$n_k = \ln(m_k - \mathrm{lb}_k), \tag{8.17}$$

where lb_k is a lower bounding constraint such that

$$m_k > \mathrm{lb}_k. \tag{8.18}$$

We also can express m_k in terms of n_k, via the expression

$$m_k = \mathrm{e}^{n_k} + \mathrm{lb}_k. \tag{8.19}$$

Hence

$$\partial m_k / \partial n_k = m_k - \mathrm{lb}_k. \tag{8.20}$$

To alter the NLCG algorithm to invert for log parameters, $\mathbf{n}$, we first split the gradient into two components which arise from the data misfit, $\nabla_{\mathrm{d}}\varphi$, and the regularization imposed upon the problem, $\nabla_{\mathrm{m}}\varphi$, where

$$\nabla\varphi = \nabla_{\mathrm{d}}\varphi + \nabla_{\mathrm{m}}\varphi. \tag{8.21}$$

We then simply scale components of the gradient arising from the first term in Equation (8.21), $\nabla_{\mathrm{d}}\varphi$, using Equation (8.20) (that is for the kth component of $\nabla_{\mathrm{d}}\varphi$ we scale it by the factor $m_k - \mathrm{lb}_k$) and replace the model parameter vector $\mathbf{m}$ by its log counterpart $\mathbf{n}$ in the NLCG algorithm.

4. MARINE MT RESOLUTION STUDY

Next we demonstrate the 3D MT inversion code capabilities with a resolution study of imaging 3D sub-salt structures, an important target in marine magnetotellurics for oil exploration. For a detailed description of the marine MT method, including the instrumentation involved and data interpretation practices, we refer readers to the works of Constable et al. (1998) and Hoversten et al. (1998, 2000). The aim of the current study is to determine if the base of salt could be better resolved using 3D data analysis compared with much faster 2D interpretation of the data along selected profiles. An additional point of the investigation is to determine where 2D analysis of the data is inappropriate due to the assumption of 2D geology. The data employed in this study were generated with the finite-difference solution discussed earlier in the paper at 13 frequencies that span the range from 0.125 to 0.0005. A 175-MHz R10000 Octane SGI workstation was employed for the forward calculations. Sections of the model are shown

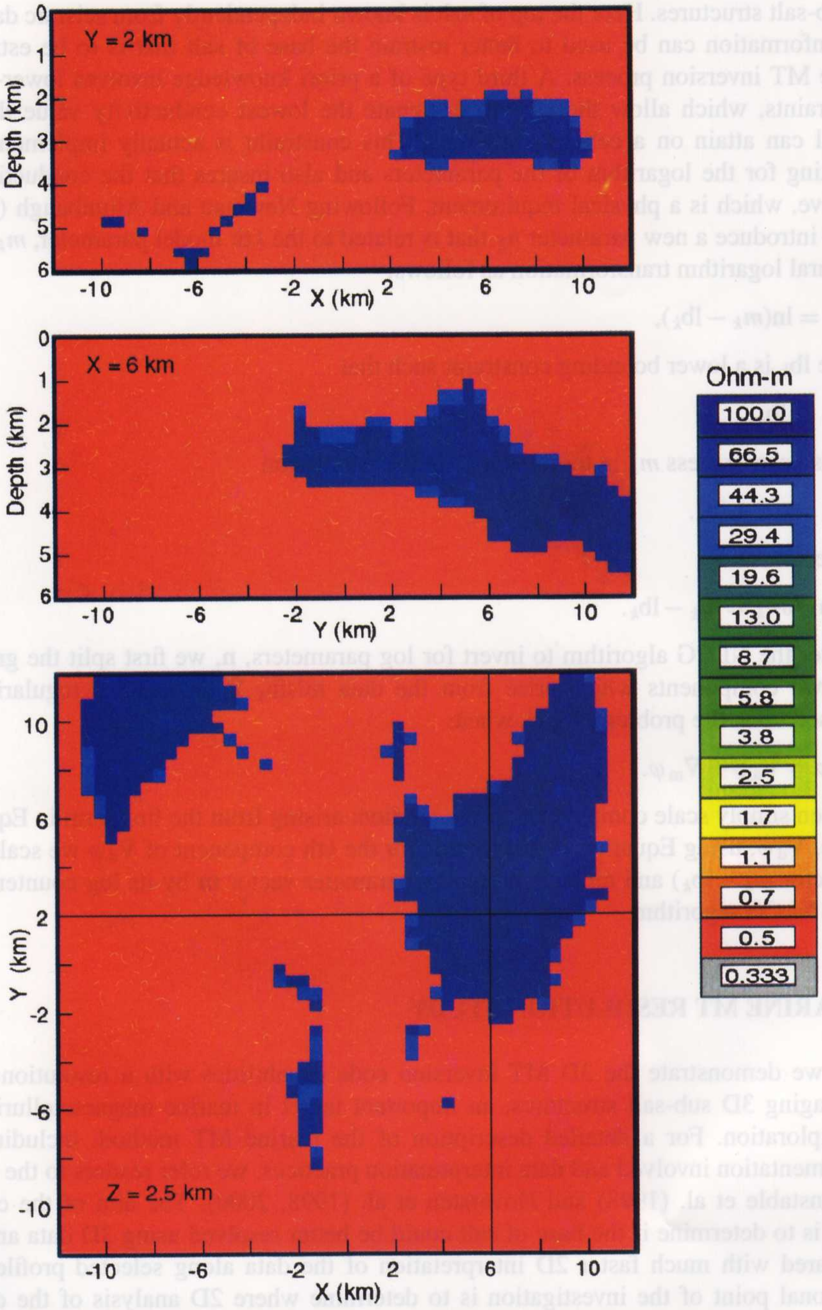

Figure 3. 3D Mahogany salt model used in seafloor MT inversion study. The top two panels show resistivity cross-sections at $Y = 2$ km and $X = 6$ km. The bottom panel illustrates the lateral geometry of the salt bodies at 2.5 km depth; note that the top flank of the salt actually terminates at $Y = 13$ km, off the top of the X–Y map section. The seawater depth is small at 100 m in the model and the seawater is assigned a resistivity of 0.333 Ω m.

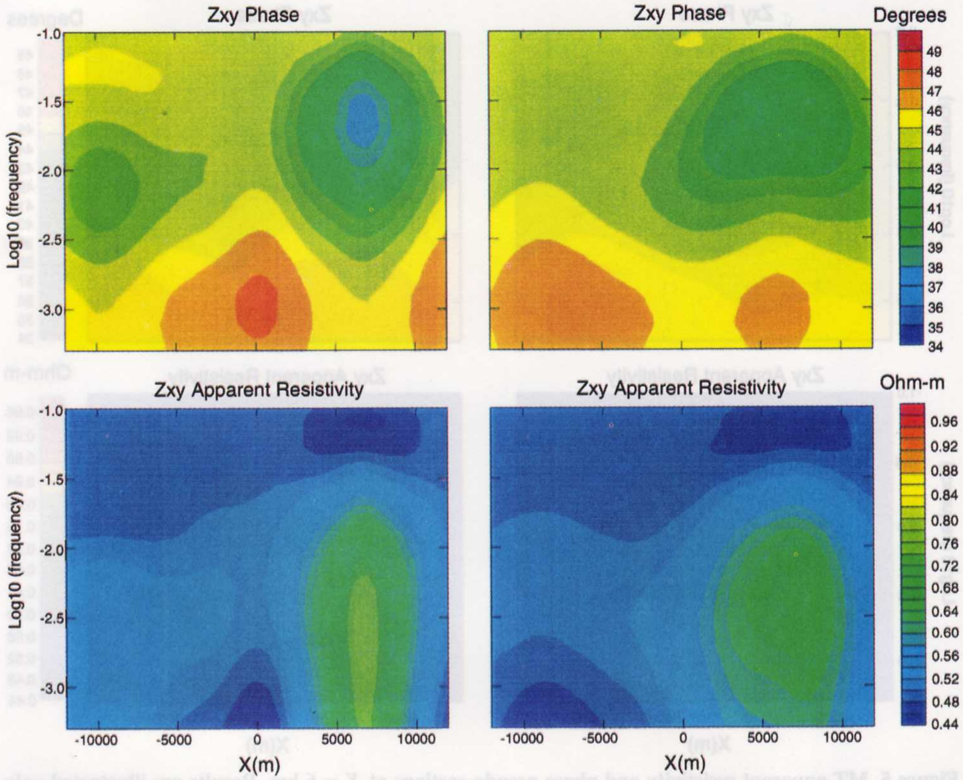

Figure 4. MT apparent resistivity and phase pseudo-sections at $Y = 2$ km. Results are illustrated only for Z_{xy} and Z_{yx} impedances.

in Figure 3, where the sea is quite shallow (100 m) and has been assigned a resistivity of 0.333 Ω m. The 100-Ω m salt structure, embedded within the 0.5-Ω m sediments, is a highly complex 3D feature, and is modeled after the Mahogany prospect, in the Gulf of Mexico. Figures 4 and 5 show selected pseudo-sections of impedance phase and resistivity. The 3D nature of the site is readily apparent in the apparent resistivity responses, which show the 3D salt bodies affecting these responses to arbitrary low frequencies in both the Z_{xy} and Z_{yx} modes. In computing these results the LIN preconditioner was very effective in accelerating the solution at the longer periods. As an example, a reduction of more than a factor of 12 was observed in the computational times at the three lowest frequencies (5×10^{-4}, 7.92×10^{-4} and 1.25×10^{-3} Hz) when compared to the solution that employed a simple Jacobi preconditioner.

Because the 3D finite-difference solution is employed within the 3D NLCG scheme, we used a finer grid in solving the inverse problem. This step insures that the inversion results will not depend upon the grid used in simulating the data, and thereby provides another check on the inversion scheme. In preparing the data for inversion, 5% Gaussian random noise based on the amplitude of the impedance at the seafloor was added to the off diagonal components of the impedance tensor. The diagonal components, Z_{xx}

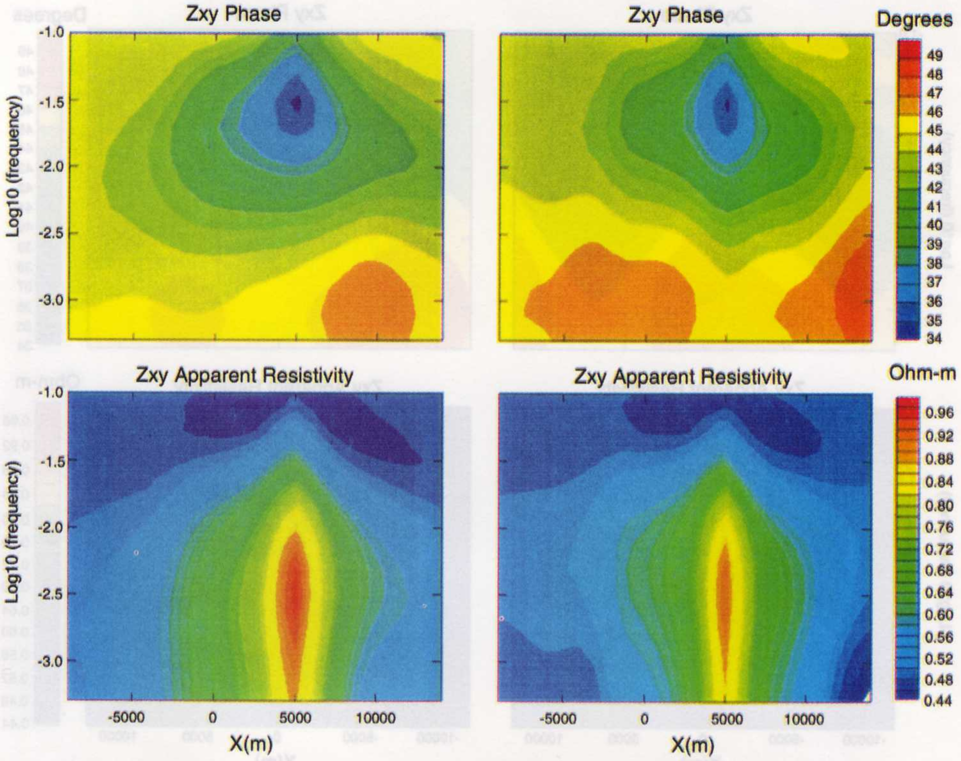

Figure 5. MT apparent resistivity and phase pseudo-sections at $X = 6$ km. Results are illustrated only for Z_{xy} and Z_{yx} impedances.

and Z_{yy}, were omitted in the analysis at all frequencies. Our justification for omitting these data values is based on the observation that they are effectively random noise in the high- to mid-frequency band of the measurement. Common sense then dictates that they be removed before analyzing field data. While it is possible to include these data values at lower-frequency bands in the analysis we have chosen not to at this time. The data set to be inverted is extremely large; 31,200 data points in survey lines that are spaced every kilometer along the X and Y coordinate directions that range from ± 12 km in X and -9 to 14 km in Y. Our justification in using this amount of data in the analysis is to determine in the ideal case the optimal image resolution one can expect from 3D inversion. Thus with the knowledge of the best imaging resolution that can be achieved for the problem, one can then construct data acquisition strategies that tradeoff model resolution against survey costs. To image the 100-Ω m salt structures within the 0.5-Ω m sediments required 129,360 model or conductivity parameters. Even with the efficiencies of the NLCG algorithm it was necessary to run this inversion simulation on Sandia National Laboratories massively parallel terraflop computer using 288 processors. The inversion was launched with a starting model consisting of seawater over 0.5 Ω m sediment. Runs using several different tradeoff parameters, demonstrated that a tradeoff parameter of 10, the smallest employed, yielded a data misfit that

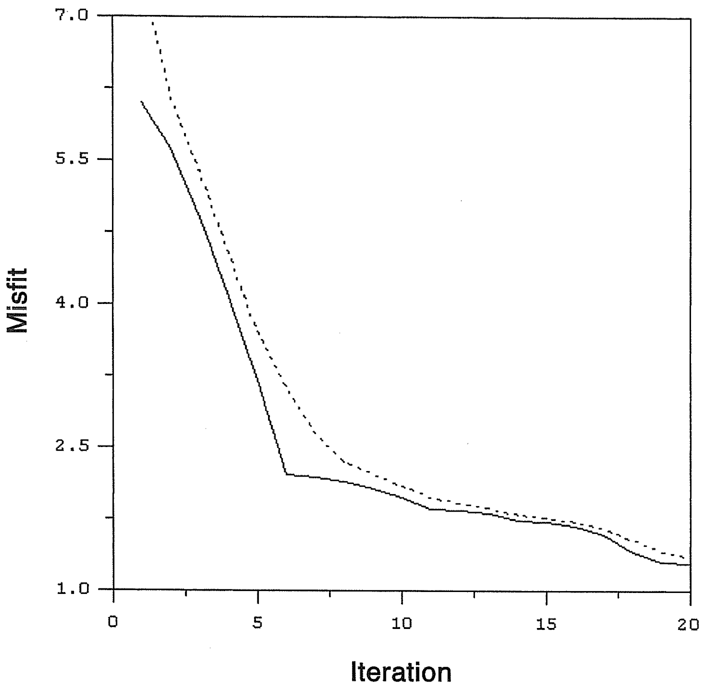

Figure 6. 3D NLCG solution convergence for the marine MT model example. The dashed curve illustrates the reduction in the cost functional (Equation 8.16) with increasing solution iteration. The solid curve represents the squared error, φ_d, where the model smoothness constraint term is omitted in the evaluation of the cost functional. The tradeoff parameter of 10 was specified to obtain these convergence results. Results show that over the first five iterations significant reduction occurs in the misfit φ.

approached the target value of 1, the assumed noise level (Figure 6); larger values yielded larger misfits and the corresponding models were rejected on that basis.

Shown in Figure 7 are cross-sections from the inverse model at 2 km intervals along the North–South direction, coinciding with the y coordinate direction in the model. Each depth section is 20 km in length and 10 km in depth. The top slice is located at $y = 0$ km and the bottom one at 12 km. To improve the resolution of these images we also incorporated a tear in the regularization matrix at the top of salt, and applied lower bounding constraints on the model parameters, but did not invert against a reference model in this example. The lower bounds on the conductivity were set at 2 and 0.01 S/m above and below the top of salt respectively, or equivalently 0.5 and 100 Ω m as upper bounds on the resistivities; because parts of the starting model coincide with the upper bounding constraint of 0.5 Ω m, we perturbed the bound to 0.55 Ω m at those points to insure that Equation (8.17) stays bounded. Incorporation of the tear and lower-bound constraints into the inverse problem is justified since seismic data provide independent estimates on depth to the top of salt.

Notice that the inversion recovers the general shape of the structures, especially at the top of the salt where we have incorporated the tear. However also notice that (1) the

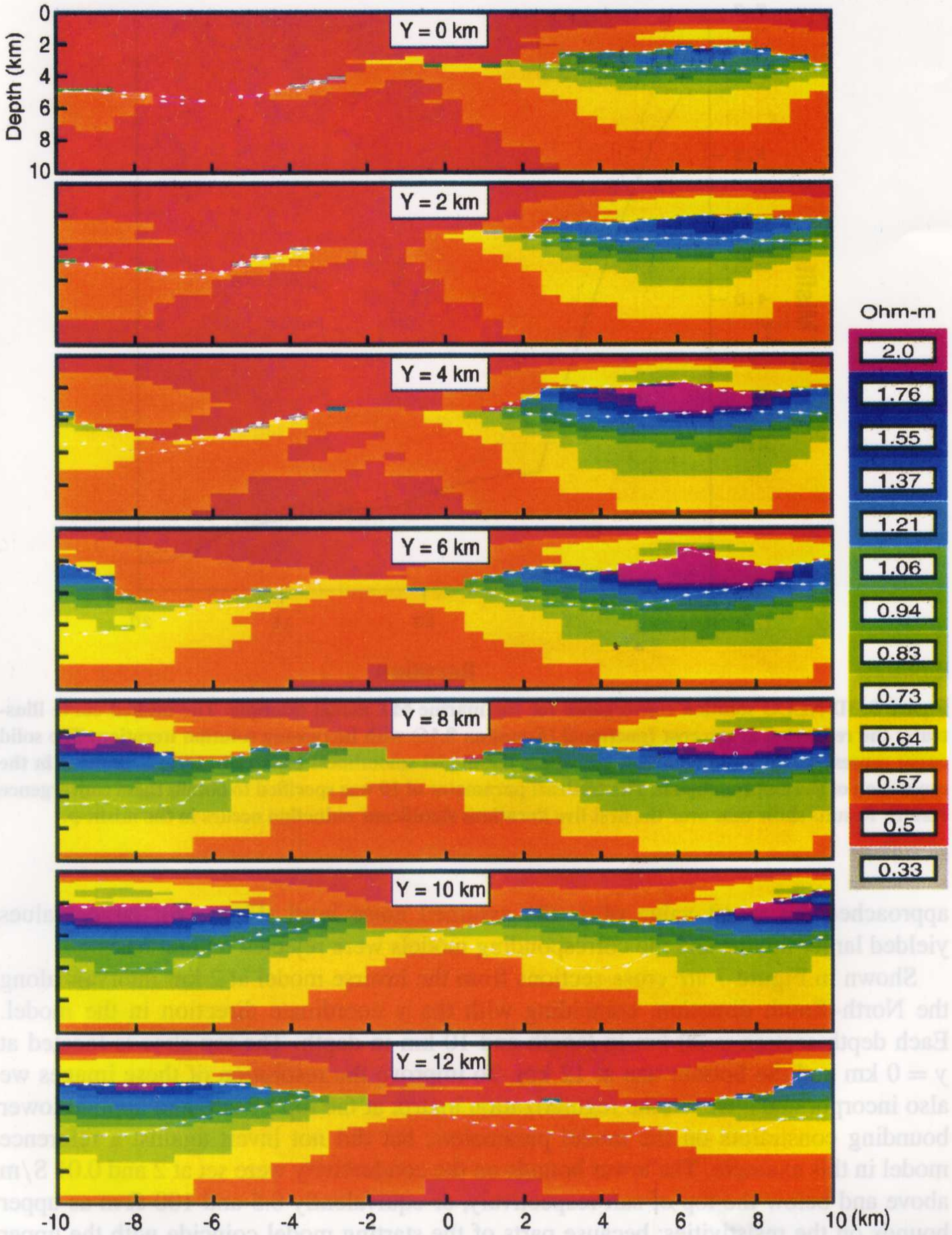

Figure 7. Illustrated here is a three-dimensional reconstruction of the Mahogany salt bodies. Seven cross-sections are illustrated at 2-km intervals along the North–South direction, starting at $Y = 0$ km at the top and ending at 12 km at the bottom. Each depth section is 20 km in length and 10 km in depth. The white lines indicate the true positions of the top and base of salt. Departures from the sediment resistivity of 0.5 Ω m indicate resistive salt features with maximum resistivity estimates of 5 Ω m.

bottom of the salt is imaged to be smoothly varying rather than a sharp interface, and (2) the highest resistivity that is recovered within the salt is well below the known value of 100 $\Omega\,$m. The first effect is to be expected due to the smoothing nature of the regularization constraints that are imposed, i.e., the problem is not set up to image the location of sharp interfaces. With regard to not being able to recover the actual resistivity of the salt, this too is to be expected as the MT response becomes saturated once the resistivity contrast is large (Hoversten et al., 1998). Fortunately, the resistivity of salt is not of interest in petroleum exploration, only its base location.

In Figure 8, the predicted impedances for the model are compared with the input data at 0.0005 Hz in map view. Figure 9 shows a pseudo-section plot of apparent resistivity and phase at $Y = 9$ km. In both cases the agreement between the predicted and input data are good, with the main difference being the presence of the random noise in the input data which is not present in the predicted results.

We have also done a series of 2D inversions on the Z_{xy} mode data along the $Y = 8$ km section (east–west line) of the 3D data set to illustrate two points. First of all we will compare 2D and 3D inversion over this section to see what if any benefits the 3D inversion offers. Note from Figure 3 and the results in Figure 7 that this profile has been chosen in a region where the structure is somewhat 2D, that is the variation in the y direction is small compared to that in the x direction. Therefore this represents a best-case scenario for 2D inversion to produce reliable results. The second point we wish to consider are the effects of the various constraints that can be imposed in resolving of the base of the salt. In this regard we have not only employed a 2D version of the 3D algorithm described in this paper, but also the Sharp2D algorithm (Smith et al., 1999). This later algorithm is ideally designed to invert for the location of boundaries between regions of different conductivity rather than for a smoothly varying model. Together, these algorithms span a range of possible constraints that can be imposed upon this type of model, and therefore serve to illustrate the considerable impact that different types of a priori knowledge can have on recovering certain features within the image (base of salt in this case).

Five different cases are illustrated in Figure 10. Figure 10a shows the model produced by 2D nonlinear conjugate gradient inversion with no constraints of any kind, and Figure 10b shows the result when a tear in the regularization is applied at the top of the salt. Figure 10c shows the inverse model generated when a tear is employed at the top of the salt along with the same upper bounds on resistivity above and below the top of salt as was used in the 3D case. Figure 10d shows the inverse model produced by the Sharp2D code (Smith et al., 1999) where not only the top of the salt location was fixed but also the sediment resistivity above the top of salt and the resistivity of the salt were fixed. The salt resistivity was fixed at 10 $\Omega\,$m, which is not equal to the true 100 $\Omega\,$m but is high enough that the MT response is already saturated. As previously discussed, increasing the salt resistivity has no meaningful effect on the observed MT responses. Finally, Figure 10e shows the 3D inverted depth section at 8 km taken from Figure 7 and re-plotted at an identical scale used for the 2D images.

It is clear from the 2D results in Figure 10 that as more information is added to the inversion in the form of top-of-salt location and bounds on the possible resistivities of different regions, the inverse model improves. When no constraints of any form are

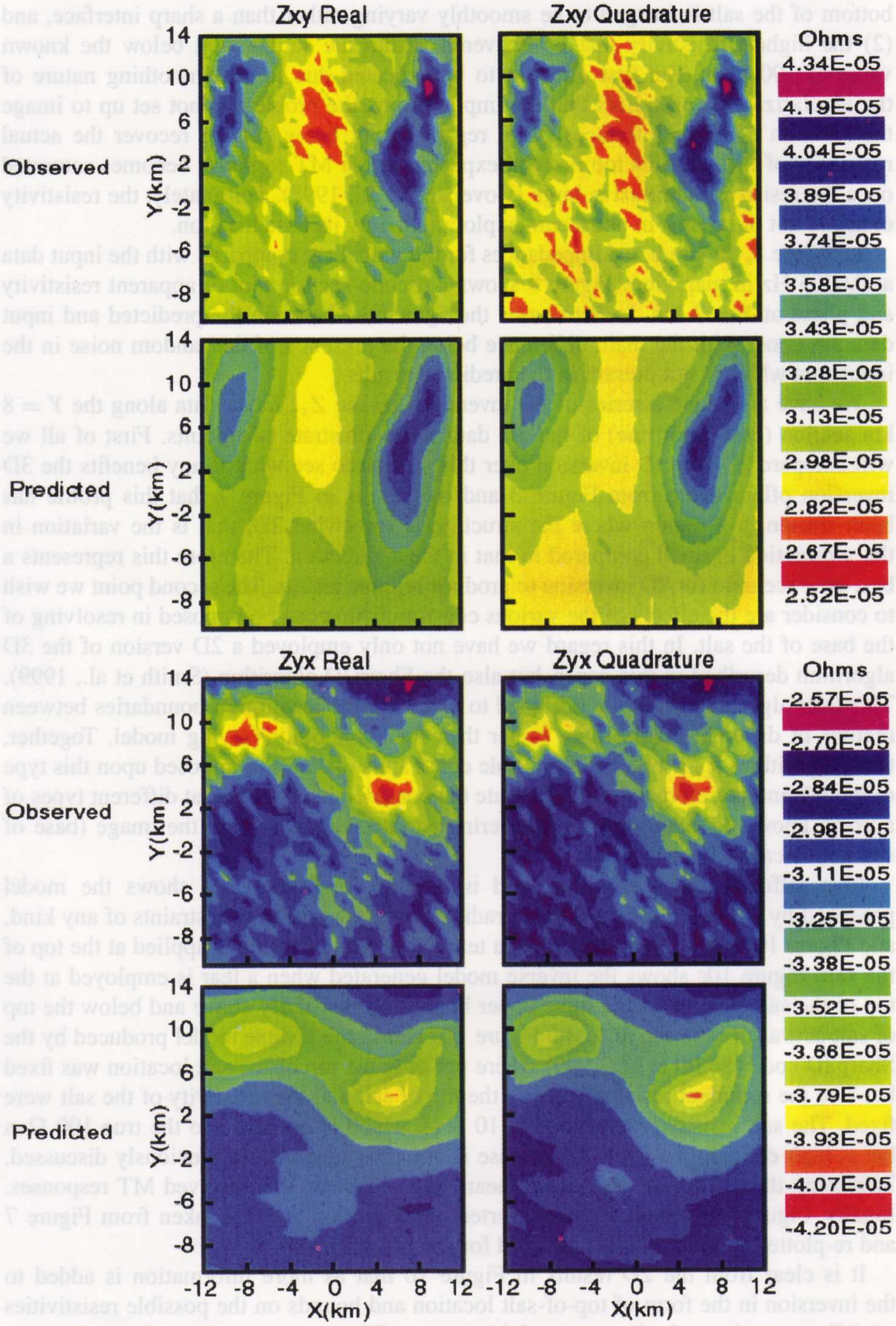
Zxy Real
Zxy Quadrature
Ohms
4.34E-05
4.19E-05
4.04E-05
3.89E-05
3.74E-05
3.58E-05
3.43E-05
3.28E-05
3.13E-05
2.98E-05
2.82E-05
2.67E-05
2.52E-05
Observed
Predicted
Y(km)
14
10
6
2
-2
-6
-8
Zyx Real
Zyx Quadrature
Ohms
-2.57E-05
-2.70E-05
-2.84E-05
-2.98E-05
-3.11E-05
-3.25E-05
-3.38E-05
-3.52E-05
-3.66E-05
-3.79E-05
-3.93E-05
-4.07E-05
-4.20E-05
X(km)
-12
-8
-4
0
4
8
12

Figure 8. Observed and predicted Z_{xy} and Z_{yx} impedance maps at 0.0005 Hz.

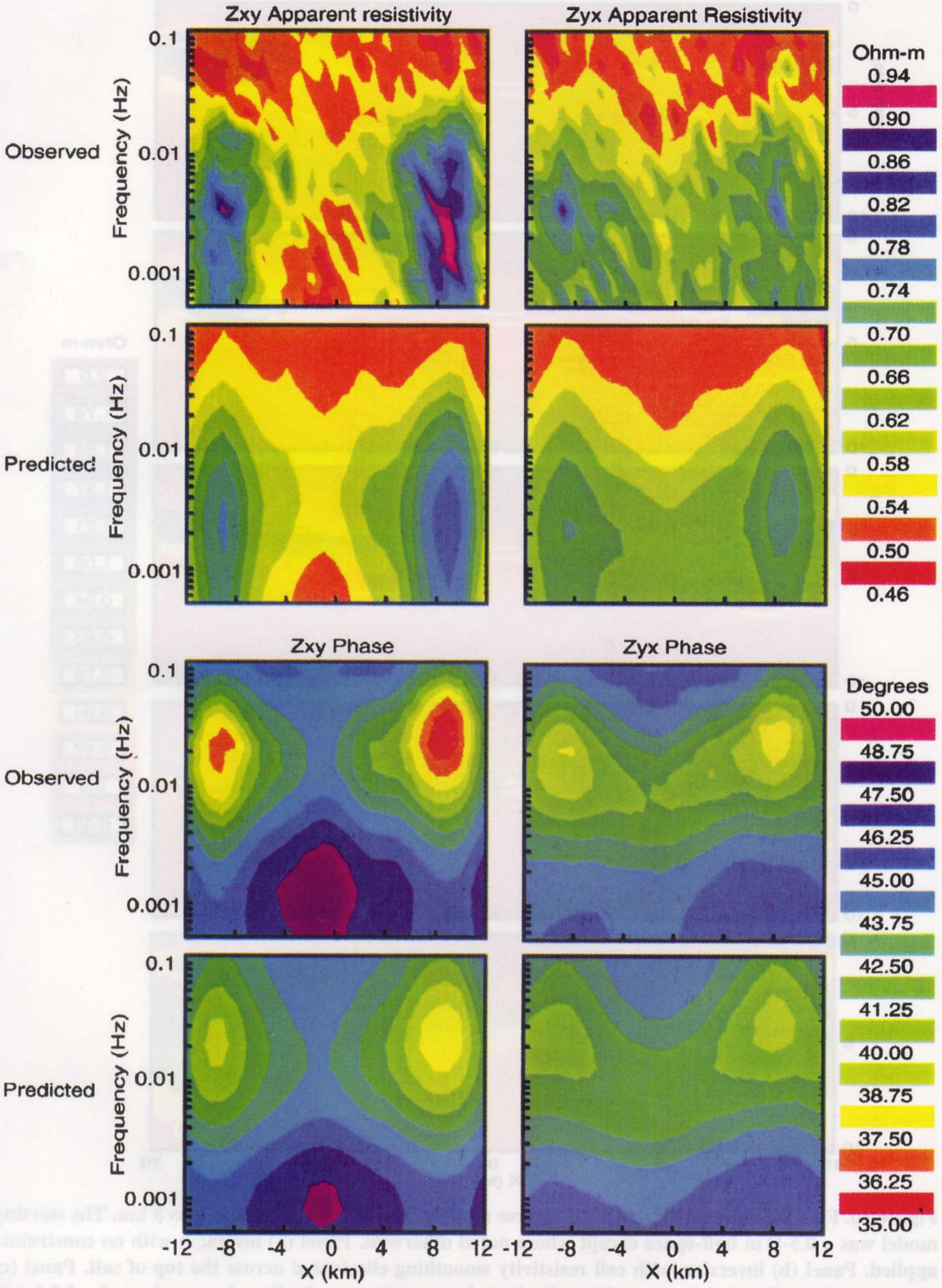

Figure 9. Observed and predicted apparent resistivity and phase soundings, based on Z_{xy} and Z_{yx} impedance data taken at $Y = 9$ km.

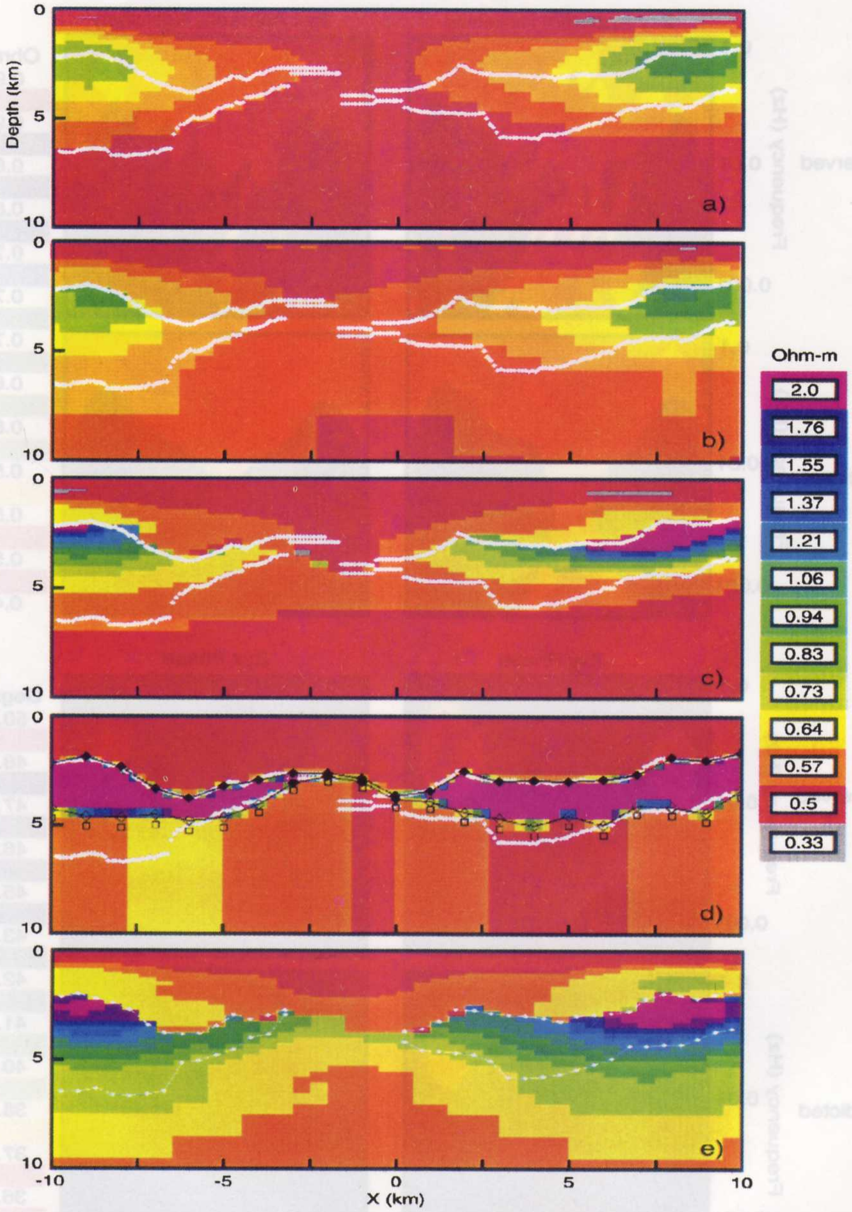

Figure 10. First four panels illustrate 2D inverse models from Z_{xy} mode data at $Y = 8$ km. The starting model was a 0.5-Ω m half-space except where noted otherwise. Panel (a) inversion with no constraints applied. Panel (b) inversion with cell resistivity smoothing eliminated across the top of salt. Panel (c) inversion with cell resistivity smoothing eliminated across the top of salt and upper bounds of 0.5 and 100 Ω m above and below the top of salt respectively. Panel (d) inversion using the Sharp2D algorithm where the resistivity above the top of salt was fixed to the true value, the top salt boundary was fixed at its true location, and the salt resistivity was fixed at 10 Ω m. Only the base of salt and the resistivity below the base of salt were sought in the inversion. Black diamonds represent boundary node locations (filled = fixed, open = variable), black open squares indicate the resistivity below the interface was free to vary. Panel (e) $Y = 8$ km section taken from 3D inversion shown in Figure 7.

used (Figure 10a) the inverse model has high-resistivity zones where the two major salt units are nearest the surface. In this case the distribution of the smoothed high-resistivity zones could lead to interpreting both the top and base of the salt as being too shallow in the section. In addition almost no indication is given of the deeper sills of salt extending from the main salt bodies on either sides into the center of the section. When the location of the top of salt is used to eliminate cell smoothing at this location the high-resistivity zones of the inverse model (Figure 10b) have moved to greater depth, better representing the true distribution. In particular, the transition in the color contours from 0.73 to 0.83 Ω m is now beginning to correctly locate the deeper and thinner salt sills in the center of the section. When the upper resistivity bounds of 0.5 and 100 Ω m, above and below the top of salt respectively, are added to the smoothing tears (Figure 10c) the image again improves. Both salt sills are now better defined when compared to Figure 10a and b.

The final case, Figure 10d, not only increases the constraints placed on the model (resistivity above salt is fixed, top salt is fixed, and salt resistivity is fixed) but also changes the parameterization of the model. Rather than cell resistivity being the parameter of the inversion, the depths of interface–nodes and the resistivity of the layer (defined at the node positions) below an interface are estimated by the inversion process. Both the boundary location and resistivity of the layer below the interface are linearly interpolated between nodes. This parameterization allows sharp jumps in resistivity across boundaries, which more closely matches the geologic model. In this particular example, only the location of the base-of-salt nodes and the resistivities below the salt were determined in the inversion. This represents a realistic case where the top salt is known from seismic data, the sediments above salt are known from well logs, and the salt itself is known to have a resistivity substantially greater than the surrounding sediments. With this amount of a priori information the inversion is able to more accurately locate the base of salt of both bodies as well as clearly define the thinner salt sills in the center of the section. However, notice that the base of the salt body on the left side of the model (the deepest salt) is not well defined by any of the four 2D examples shown here. Thus this either represents a portion of the model which the data is not sensitive to, or a location where 3D effects distort the 2D inversion results.

To compare 2D and 3D inversion results, consider the $Y = 8$ km panel of Figure 7 redrawn as Figure 10e, which should be compared directly with Figure 10c. The same basic inversion algorithm and constraints were used in both cases with the only difference being the dimensionality that is assumed. Remember from Figure 3 that although this profile crosses a region where the variation in the y direction is minimal compared to other areas within the model, there is still significant 3D structure present and thus there will be 3D effects in the data.

In general the two inversion results appear to yield much of the same information. However the 3D inverse model (Figure 10e, $Y = 8$ km) appears to do a better job of indicating the presence and base location of both salt sills in the center of the section than does the 2D inverse model (Figure 10c). In particular, the thin salt sill extending to the center from the left side body is well imaged in the 3D model compared to the 2D model. An argument could also be made that the 3D inverse model better represents the base of the left side salt body better than any of the 2D inversions shown in Figure 10.

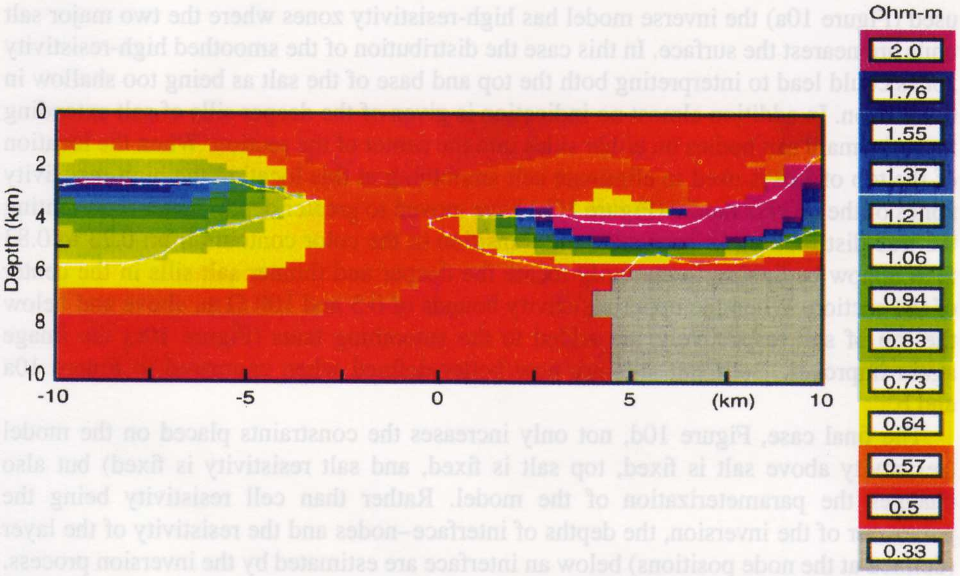

Figure 11. Two-dimensional inverse model from Z_{xy} and Z_{yx} mode data taken over the edge of the salt flank at $Y = 12.5$ km.

However also note that the 2D inversion appears to better represent the right side body toward the $X = 10$ km edge of the inversion mesh than the 3D inversion results.

Nevertheless 2D inversion requires careful selection of data profiles to insure that 3D lateral effects are minimized. A poor selection can produce artifacts as Figure 11 demonstrates. Here the profile selected to be inverted is situated at $Y = 12.5$ km, over the lateral flanks of the salt structures; note that the salt flanks actually extend out to $Y = 13$ km in the lower section of Figure 3. Following the recommendation of Berdichevsky et al. (1998), both Z_{xy} and Z_{yx} modes were used in the inversion to insure the most reliable determination of the subsurface geology, especially given the resistive nature of the 3D salt bodies. While the base of salt is imaged exceedingly well, an artifact appears below the salt in the lower right side of the image. This artifact represents a 34% deviation from the sea sediments and could be erroneously interpreted as an important geological structure. However, one could argue, given the subtle nature of the artifact, this would not lead to a serious misinterpretation of the geology. Nevertheless, this result clearly shows the benefit of 3D inversion, since the corresponding 3D image at 12 km in Figure 7 shows no such artifact and does a reasonable job in imaging the salt.

While 3D inversion results and carefully selected 2D inversion profiles are encouraging, images of the base of salt are not as sharp as would be desired. This finding is somewhat discouraging for 3D data analysis given the amount and coverage of the data employed in the 3D analysis. On the other hand, it suggests that the 3D inversion could be made with fewer sounding locations, given the good results obtained using 2D data analysis. Nevertheless, we are currently investigating additional constraints that can be incorporated into the problem to improve the base salt resolution. The ability to place arbitrary upper and lower bounds on different regions of the model as well as fixing resistivities over portions of the model (comparable to the Sharp2D example) would clearly be beneficial in cases like these.

5. CONCLUSIONS

In this paper we reviewed techniques to model and invert MT data in three dimensions with application to modeling and imaging salt structures, an important target in marine magnetotellurics. To accelerate 3D finite-difference modeling at long periods, we have also introduced a fast preconditioner that is based upon an approximate solution of Maxwell's equations at low induction numbers. Test examples clearly show the benefit of the preconditioner, where an order of magnitude speed up in solution time has been demonstrated on a series of test problems. The unique feature of the preconditioner is its ability to deflate out the effect of the null space of the discrete curl–curl operator in the Krylov solution process. When this null space is active, it is responsible for the poor convergence properties of the forward-modeling solution at long periods.

The resolution analysis has shown that 3D inversion, with carefully crafted constraints that incorporate a priori information, will offer somewhat improved resolution compared to corresponding 2D analysis. Whether the marginal improvements in resolution are cost effective is debatable given the time and amount of high-quality data needed for 3D data inversion. On the other hand, care must be exercised, when interpreting 3D data sets with 2D inversion schemes. As has been demonstrated improperly chosen profiles over the salt flanks, can produce 3D artifacts within the 2D model. While such artifacts are subtle in nature, they have only been observed over the salt flanks and not over the center of the resistive salt bodies. Thus it appears that these artifacts are caused by the assumptions in the 2D modeling and inversion algorithms not being fully able to incorporate the 3D nature of the data.

In spite of our findings on the marginal improvements demonstrated here with 3D data analysis, we believe that with increasing computer power and new algorithms 3D MT modeling and inversion will see increasing use within the induction community. One can well imagine a situation where 3D effects are so severe that proper analysis of the data requires full 3D treatment. Thus the solution techniques presented in this paper are a step in this direction. More importantly, with the incorporation of constraints in the inversion process, 3D MT modeling and inversion offers the potential to realistically image complex geological systems of economic and academic interest.

ACKNOWLEDGEMENTS

We wish to acknowledge the numerous discussions with David Day on solution preconditioning and the critique of Andreas Hördt, which improved the paper. This work was performed at Sandia National Laboratories, Lawrence Berkeley National Laboratory and the University of Cologne in the Federal Republic of Germany. Funding provided by the United States Department of Energy's Office of Basic Energy Sciences, Division of Engineering and Geoscience and a Mercator grant awarded to G.A. Newman from the Deutsche Forschungsgemeinschaft. Sandia is a multi-program laboratory operated by the Sandia Corporation, a Lockheed Martin Company, for the United States Department of Energy under Contract DE-AC04-94AL85000.

Appendix A

It is possible to generalize the LIN preconditioner and provide a rigorous bound of its effectiveness by recasting the solution of Equation (8.2) as

$$\mathbf{E} = (\mathbf{I} + i\omega\mathbf{A}^{+}\mathbf{D})^{-1}\mathbf{A}^{+}\mathbf{S}. \tag{8.A1}$$

The matrices $\mathbf{I}$, $\mathbf{A}$ and $\mathbf{D}$ are matrices that represent the identity, the discrete curl–curl operator and attenuation terms in Equation (8.A1), where

$$\mathbf{K} = \mathbf{A} + i\omega\mathbf{D}. \tag{8.A2}$$

The matrix $\mathbf{D}$ is also diagonal with real elements and $\mathbf{A}^{+}$ represents the pseudo-inverse of $\mathbf{A}$, such that $\mathbf{A}^{+}\mathbf{A} = \mathbf{I}$ only over those vectors not included in the null space of $\mathbf{A}$; that is for some vector, $\mathbf{v}$, orthogonal to this null space, we have $\mathbf{A}^{+}\mathbf{A}\mathbf{v} = \mathbf{v}$. Matrix–vector products involving the pseudo-inverse, $\mathbf{A}^{+}\mathbf{S}$, are determined by solving discrete versions of Equations (8.10) and (8.12) with appropriate boundary conditions, included explicitly in $\mathbf{S}$. A Neumann series expansion of Equation (8.A1) (cf. Golub and Van Loan, 1989) can formally be written as

$$\mathbf{E} = \sum_{n=0}^{\infty}\{-i\omega\mathbf{A}^{+}\mathbf{D}\}^{n}\mathbf{A}^{+}\mathbf{S}, \tag{8.A3}$$

where the LIN preconditioner would be based on using only the first term in the series. This series will converge provided the spectral radius, denoted by ρ, is less than one, where

$$\rho(\omega\mathbf{A}^{+}\mathbf{D}) < 1. \tag{8.A4}$$

The spectral radius corresponds to the largest eigenvalue of $||\omega\mathbf{A}^{+}\mathbf{D}||$ and its evaluation will provide a measure under the worst possible conditions when the series will converge and the preconditioner will be effective. Unfortunately evaluation of Equation (8.A4) requires the solution of an eigenvalue problem, which is computationally impractical. Nevertheless an estimate of the spectral radius is readily available if we assumed that the conductivity and grid size is constant in the modeling problem. We can then estimate the spectral radius using the smallest non-zero eigenvalue of $\mathbf{A}$ following Newman and Alumbaugh (2002) as

$$\rho(\omega\mathbf{A}^{+}\mathbf{D}) \approx \omega\mu_{o}\sigma L_{\max}^{2}/2\pi^{2}, \tag{8.A5}$$

where $L_{\max}$ is the largest dimension employed in the 3D finite-difference grid. Equation (8.A5) clearly indicates that as frequency is decreased sufficiently, acceleration in the convergence rate of the Neumann series, and an increase in the effectiveness of the preconditioner will be observed. In a final remark, Equation (8.A3) can also be used to develop a higher-order LIN preconditioner at the expense of evaluating more terms in the series.

REFERENCES

Avdeev, D.B., Kuvshinov, A., Prankratov, O.V. and Newman, G.A., 2002. Three-dimensional induction logging problems, Part I: An integral equation solution and model comparisons. Geophysics, 67, 413–426.

Alumbaugh, D.L., Newman, G.A., Prevost, L. and Shadid J.N., 1996. Three-dimensional wide band electromagnetic modeling on massively parallel computers. Radio Sci., 31, 1–23.

Berdichevsky, M.N., Dmitriev, V.I. and Pozdnjakova, E.E., 1998. On two-dimensional interpretation of magnetotelluric soundings. Geophys. J. Int., 133, 585–606.

Constable, S.C., Orange, A.S., Hoversten, G.M. and Morrison, H.F., 1998. Marine magnetotellurics for petroleum exploration Part I: A sea floor equipment system. Geophysics, 63, 816–825.

DeGroot-Hedlin, C. and Constable, S.C., 1990. Occam's inversion to generate smooth two-dimensional models from magnetotelluric data. Geophysics, 55, 1613–1624.

Druskin, V.L., Knizhnerman and Lee, P., 1999. New spectral Lanczos decomposition method for induction modeling in arbitrary 3D geometry. Geophysics, 64, 701–706.

Egbert, G.D. and Booker, J.R., 1986. Robust estimation of geomagnetic transfer functions. Geophys. J. R. Astron. Soc., 87, 173–194.

Fletcher, R. and Reeves, C.M., 1964. Function minimization by conjugate gradients. Comput. J., 7, 149–154.

Frischknecht, F.C., 1987. Electromagnetic physical scale modeling. In: M.N. Nabighain (Ed.), Electromagnetic Methods in Applied Geophysics – Theory, Vol. 1. Soc. Explor. Geophys., Tulsa, OK, pp. 131–311.

Gamble, T.D., Goubau, W.M. and Clarke, J., 1979. Magnetotellurics with a remote reference. Geophysics, 44, 53–68.

Golub, G. and Van Loan, J., 1989. Matrix Computations. John Hopkins University Press, Baltimore, MD.

Greenbaum, A., 1997. Iterative methods for solving linear systems. Society for Industrial and Applied Mathematics, Philadelphia, PA.

Hestenes, M.R. and Stiefel, E., 1952. Methods of conjugate gradients for solving linear systems. J. Res. Natl. Bur. Stand., 49, 409–436.

Hoversten, G.M., Morrison, H.F. and Constable, S., 1998. Marine magnetotellurics for petroleum exploration Part 2: Numerical analysis of subsalt resolution. Geophysics, 63, 826–840.

Hoversten, G.M., Morrison, H.F. and Constable, S.C., 2000. Marine magnetotellurics for base salt mapping: Gulf of Mexico field test at the Gemini structure. Geophysics, 65, 1476–1488.

Newman, G.A. and Alumbaugh, D.L., 1995. Frequency-domain modeling of airborne electromagnetic responses using staggered finite differences. Geophys. Prospect., 43, 1021–1042.

Newman, G.A. and Alumbaugh, D.L., 2000. Three-dimensional magnetotelluric inversion using nonlinear conjugate gradients. Geophys. J. Int., 140, 410–424.

Newman, G.A. and Alumbaugh, D.L., 2002. Three-dimensional induction logging problems, Part II: A finite difference solution. Geophysics, 67, 484–491.

Polyak, E. and Ribière, G., 1969. Note sur la convergence des méthods conjugées. Rev. Fr. Inr. Rech. Oper., 16, 35–43.

Rodi, W. and Mackie, R.L., 2001. Nonlinear conjugate gradients algorithm for 2D magnetotelluric inversion. Geophysics, 66, 174–187.

Siripunvaraporn, W. and Egbert, G., 2000. An efficient data–space inversion for two-dimensional magnetotelluric data. Geophysics, 65, 791–803.

Smith, J.T., 1996. Conservative modeling of 3-D electromagnetic fields; Part II: Biconjugate gradient solution and an accelerator. Geophysics, 61, 1319–1324.

Smith, J.T. and Booker, J.R., 1991. Rapid inversion of two- and three-dimensional magnetotelluric data. J. Geophys. Res., 96, 3905–3922.

Smith, J.T., Hoversten, G.M., Gasperikova, E. and Morrison, H.F., 1999. Sharp boundary inversion of 2-D magnetotelluric data. Geophys. Prospect., 47, 469–486.

Tikhonov, A.N. and Arsenin, V.Y., 1977. Solutions to Ill-Posed Problems. Wiley, New York, NY.

Vozoff, K., 1991. The magnetotelluric method. In: M.N. Nabighain (Ed.), Electromagnetic Methods in Applied Geophysics – Applications, Vol. 2. Soc. Explor. Geophys., Tulsa, OK, pp. 641–712.

Xiong, Z., 1992. Electromagnetic modeling of 3-D structures by the method of system iteration using integral equations. Geophysics, 57, 1556–1561.

Yee, K.S., 1966. Numerical solution of initial boundary value problems involving Maxwell's equations in isotropic media. IEEE Trans. Antennas Propagation, AP-14, 302–309.